Uniaxially aligned 1D sandwich-molecular wires: electronic structure and magnetism

Stefan Kraus,*,† Alexander Herman,‡ Felix Huttmann,† Marco Bianchi,¶ Raluca-Maria Stan,¶ Ann Julie Holt,¶ Shigeru Tsukamoto,§ Nico Rothenbach,‡ Katharina Ollefs,‡ Jan Dreiser,∥ Ken Bischof,† Heiko Wende,‡ Philip Hofmann,¶ Nicolae Atodiresei,§ and Thomas Michely†

†II. Physikalisches Institut, Universität zu Köln, Zülpicher Str. 77, 50937 Köln, Germany ‡Faculty of Physics and Center for Nanointegration Duisburg-Essen (CENIDE), University of Duisburg-Essen, Lotharstraße 1, 47048 Duisburg, Germany

¶Department of Physics and Astronomy, Interdisciplinary Nanoscience Center (iNANO),

Aarhus University, 8000 Aarhus C, Denmark

§Peter Grünberg Institute and Institute for Advanced Simulation, Forschungszentrum

Jülich, Wilhelm-Johnen-Straße, 52428 Jülich, Germany

|| Swiss Light Source, Paul Scherrer Institute, Forschungsstrasse 111, 5232 Villigen PSI,
Switzerland

E-mail: kraus@ph2.uni-koeln.de(experiment);n.atodiresei@fz-juelich.de(theory)

Abstract

Sandwich-molecular wires consisting of europium and cyclooctatetraene (Cot) were grown in situ on the moiré of graphene with Ir(110). The moiré templates a uniaxial alignment of monolayer EuCot nanowire carpets and multilayer films with the EuCot wire axis along the [001] direction of the Ir substrate. Using angle-resolved photoemission spectroscopy we investigate the band structure of the wire carpet films. While π -derived bands were not observed experimentally, we find a flat band 1.85 eV below the Fermi energy. Using density-functional theory, X-ray photoelectron spectroscopy, and by replacing europium through barium in the sandwich-molecular wires, it is concluded that the flat band is derived from Eu 4f states weakly mixed with Eu 5d states and slightly overlapping with Cot π -states. X-ray magnetic circular dichroism is employed to characterize the magnetic properties of the EuCot wire carpet films at low temperatures. Clear evidence for an easy axis magnetization along the wires is found.

Introduction

On-surface organometallic chemistry investigates the interaction of a wide variety of metal atoms with organic molecules on a supporting layer. Due to the relevance for spintronic applications, the interaction of magnetic metal atoms — such as transition or rare-earth metals — with the surrounding ligand field of the molecules, is of specific interest. The most studied systems to date are zero-dimensional single-molecule magnets 2-10 showing a magnetic hysteresis without long-range order, and two-dimensional (2D) metal—organic networks, 11-15 some of which have been shown to mediate magnetic interaction within the surface plane. 16-20 Far less investigated are one-dimensional (1D) organometallic systems. Sandwich-molecular wires — chains of metal atoms and cyclic molecules in alternating sequence — are a class of such 1D organometallic systems. One example are transition-metal-benzene complexes, some of which have been theoretically predicted to be ferromagnetic half metals, 21-24 i.e. they can

act as spin filters. Half-metal and spin-filter properties have also been discussed by theory for transition-metal-cyclopentadien complexes, ^{25–27} or complexes containing larger molecules such as cyclononatetraenyl²⁸ or metallofullerenes. ²⁹ Recently, also cyclopentadienyl-titanium-cyclooctatetraene double deckers have even been discussed in the context of molecular spin qbits. ³⁰

Here, we focus on sandwich-molecular wires consisting of an alternating sequence of lanthanide (Ln) atoms and the eight-membered carbon ring cyclooctatetraene (C_8H_8 , Cot). $^{31?}$? $^{-33}$ While the charge-neutral Cot molecule is anti-aromatic and non-planar, it becomes aromatic and planar upon accepting two electrons. By forming a 1D chain of alternating Ln^{2+} cations and Cot^{2-} anions, elongated LnCot sandwich-molecular wires can grow. Using europium (Eu) as lanthanide metal, in gas-phase experiments wire lengths of up to 30 formula units were reported. To uncover the binding mechanism, angle-integrated photoelectron spectroscopy of gas phase wires was conducted, 31,32,34 while Stern-Gerlach experiments revealed a magnetic moment of $7\,\mu_{\rm B}$ per Eu atom, and the total magnetic moment increases linearly with the chain length. Theory has investigated the electronic and magnetic structure of short and long EuCot wires $^{35-38}$ or versions with a slightly modified Cot ring. These theoretical investigations agree in the prediction of ferromagnetic coupling and a semiconducting nature of the EuCot wires.

In situ on-surface synthesis of EuCot wires has been recently demonstrated on Gr/Ir(111). 40 This synthesis method yields wire lengths of the order of 1000 formula units. The wires interlock to form wire carpets or wire spirals. Wires on graphene (Gr) were confirmed to be ferromagnetic semiconductors 41 and are a first case of a 1D organometallic structure coupling only through van der Waals interaction to their substrate. The orientation of the EuCot wire carpet islands on Gr/Ir(111) is random in-plane. This randomness hindered not only the full determination of magnetic anisotropies, but also a measurement of the band structure of the wires which is expected to show dispersion along the wire axis.

With the present work we provide a new twist to the problem and thereby advance pre-

vious investigations on the magnetic and electronic structure of EuCot nanowires.⁴¹ Using the uniaxial moiré of graphene on $Ir(110)^{42}$ to template a unique orientation of the EuCot nanowire carpets, access to the full anisotropic electronic and magnetic properties of these 1D objects and their 2D arrangement in wire carpets is obtained.

Previous angle-resolved photoemission spectroscopy (ARPES) investigations were providing information on the highly anisotropic or one dimensional electronic band structure were successfully conducted on organic single crystals $^{43-46}$ and π -conjugated covalently-bonded 1D polymers resting on vicinal Ag or Au surfaces $^{47-49}$ and Cu(110). 50 ARPES of 1D organometallic systems was not yet conducted in the past and is presented here.

Methods

Scanning tunneling microscopy (STM) measurements and in situ sample synthesis were conducted in Cologne in the ultrahigh vacuum system ATHENE with a base pressure below $1 \cdot 10^{-10}$ mbar. In this system Gr on Ir(110) or Ir(111) was synthesized in situ. Gases are delivered through a gas dosing tube giving rise to a pressure enhancement by a factor of 80 compared to the pressure measured through a distant ion gauge and specified here. Sample cleaning was accomplished by exposure to $1 \cdot 10^{-7}$ mbar oxygen at 1200 K when needed, cycles of noble gas sputtering (Ar, Xe), and brief annealing to 1500 K. Closed layers of the single-domain Gr phase were grown on Ir(110) by exposure to $2 \cdot 10^{-7}$ mbar ethylene at 1500 K for 210 s. On Ir(111), Gr was grown by room temperature exposure to ethylene until saturation coverage was reached and subsequent thermal decomposition at 1500 K, resulting in well-oriented Gr islands, which are grown to a complete layer through an additional exposure $1 \cdot 10^{-7}$ mbar ethylene for 600 s at 1200 K.⁵¹ EuCot sandwich-molecular wires were grown on Gr/Ir(110) by sublimation of elemental Eu from a Knudsen cell with a deposition rate of $1.1 \cdot 10^{17}$ atoms in a background pressure of $1 \cdot 10^{-8}$ mbar Cot for 30 s.

STM imaging was conducted at 300 K with a sample bias and tunneling current in the order

of $U_{\rm bias} \approx -2\,{\rm V}$ and $I_{\rm t} \approx 0.1\,{\rm nA}$. For STM image processing the software WSxM 52 was applied.

To ensure Gr quality and for structural characterization low-energy electron diffraction (LEED) was used in an energy range of $30 - 150 \,\text{eV}$. LEED patterns are contrast-inverted for better visibility.

ARPES measurements were conducted at the SGM-3 beamline at the synchroton ASTRID2 in Aarhus, ⁵³ Denmark at a sample temperature of 35 K. The samples were grown in situ in an ultrahigh vacuum chamber (base pressure $3 \cdot 10^{-10}$ mbar) connected to the beamline, and using the recipe as described above. Sample cleaning was accomplished by noble gas sputtering using Ne. The samples were checked in situ using the Aarhus STM mounted at the endstation for consistency with the homelab results. For the ARPES measurements, an approximate photon (ph) flux of $5 \cdot 10^{12} \frac{\text{ph}}{\text{s}}$ was used. The total photon exposure in $\frac{\text{ph}}{\text{nm}^2}$ is specified for each data set shown and calculated as the product of photon flux, beam size on the sample $(190 \times 90 \,\mu\text{m}^2)$ and total irradiation time.

X-ray photoelectron spectroscopy (XPS) measurements were conducted at the University Duisburg-Essen for samples grown in situ using the recipe described above. EuCot (BaCot) multilayers on Gr/Ir(111) were grown by sublimation of elemental Eu (Ba) from a Knudsen cell with a deposition rate of $1.3 \cdot 10^{15} \frac{\text{atoms}}{\text{m}^2 \text{s}}$ (3.1 · $10^{15} \frac{\text{atoms}}{\text{m}^2 \text{s}}$) in a background pressure of $5 \cdot 10^{-7}$ mbar Cot (without gas dosing tube) for 2700 s (1380 s). For the XPS measurements of the multilayer films a photon energy of 1486.6 eV (Al K- α) was used. The EuCot and BaCot monolayer films on Gr/Ir(111) were checked with LEED and display diffraction rings consistent with the formation of sandwich-molecular wire carpets. ⁴⁰

X-ray absorption spectroscopy (XAS) and X-ray magnetic circular dichroism (XMCD) measurements have been conducted at the X-Treme beamline and endstation at the Swiss Light Source synchrotron in Villigen, Switzerland.⁵⁴ The samples were prepared *in situ* in an ultrahigh vacuum chamber with a base pressure of $4 \cdot 10^{-10}$ mbar directly connected to the endstation and using the recipe described above. During syntheses, sample cleaning was

achieved by oxygen etching and noble-gas sputtering using argon. For consistency with homelab results, the prepared samples were checked with LEED and a variable-temperature STM. The presented XAS data were recorded at a sample temperature of 3K and using circularly polarized light in the energy range of $1110-1250\,\mathrm{eV}$, using the total electron yield detection mode. In order to reduce irradiation damage during measurements, the beam spot size on the sample was defocussed to $0.3\times2.5\,\mathrm{mm}^2$ and the approximate photon flux was $\approx 3\cdot10^{-3}\,\frac{\mathrm{ph}}{\mathrm{nm}^2\mathrm{s}}$.

Our first-principles spin-polarized calculations were performed using the density functional theory (DFT)⁵⁵ and the projector augmented plane wave method⁵⁶ as implemented in the VASP code. 57,58 For the plane wave expansion of the Kohn-Sham wave functions 59 we used a cutoff energy of 500 eV. For the EuCot monolayer, the Brillouin zone was sampled with a $(46 \times 8 \times 1)$ k-point mesh, i.e. 46 k-points in the direction of the EuCot wire and 8 k-points in the direction perpendicular to the EuCot (BaCot) wires. We carried out the structural relaxation using the vdW-DF2⁶⁰ with a revised Becke (B86b) exchange⁶¹⁻⁶³ functional to properly account for the nonlocal correlation effects like van der Waals interactions. The analysis of the electronic structures was done using the PBE exchange-correlation energy functional.⁶⁴ We used the GGA + U approach 65 to correctly account for the orbital dependence of the Coulomb and exchange interactions of the Eu 4f states. We performed several simulations in which we varied systematically the Hubbard parameter (U_{eff}) from $3.5-7.2\,\text{eV}$. The supercell contained 15 Å of vacuum in the z direction. The EuCot and BaCot monolayers were modeled with an intra-wire periodicity of 4.35 Å and an inter-wire spacing of 6.80 Å. The DFT calculations do not include the Gr/Ir(110) substrate. The mismatch of the wire carpet with the already large moiré supercell of $\mathrm{Gr/Ir}(110)^{42}$ would require an even larger DFT supercell, for which calculations would become unfeasible.

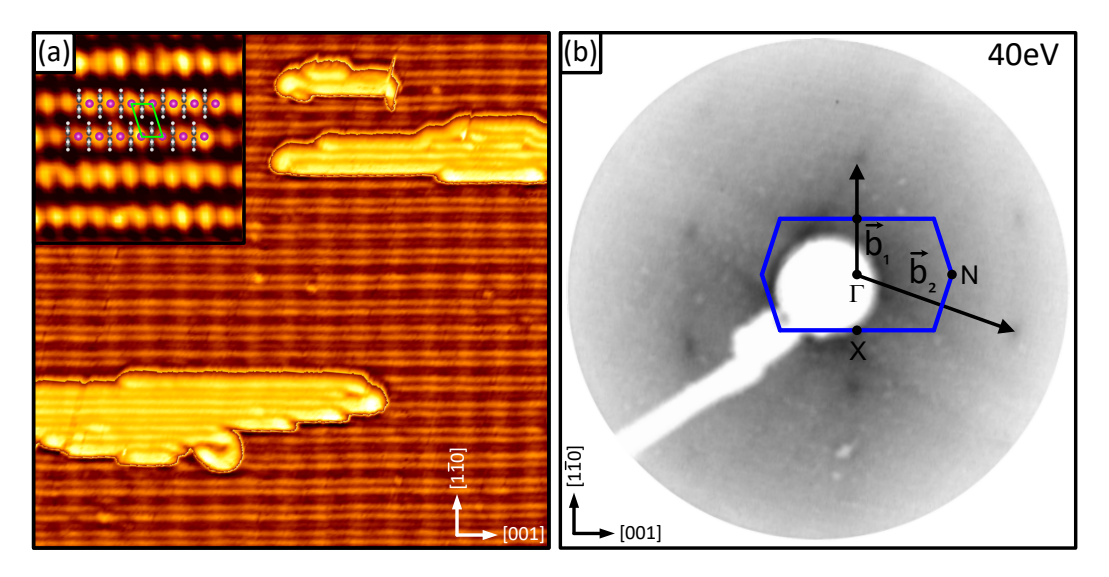


Figure 1: (a) STM topograph $(400 \times 400 \text{ Å}^2)$ of an EuCot wire carpet on Gr/Ir(110) aligned along the [100] direction with second layer wire islands aligned in the same direction. Inset: molecular resolution STM topograph $(45 \times 45 \text{ Å}^2)$ of the first layer wire carpet overlaid with a EuCot wire model. Magenta dots: Eu atoms. White and black dots: H atoms and C atoms of Cot. The wire carpet unit cell is indicated as green rhomboid. (b) 40 eV LEED pattern of a 5 ML EuCot film on Gr/Ir(110). The first Brillouin zone of the 2D wire carpet with high symmetry points X, Γ and N is indicated in blue. The reciprocal lattice vectors $\vec{b_1}$ and $\vec{b_2}$ of the wire carpet are indicated by black arrows. Tunneling parameters for (a) are $U_{\text{bias}} = -2.6 \text{ V}$ and $I_{\text{t}} = 0.06 \text{ nA}$ and the topograph is superimposed with its derivative for better visibility.

Results and discussion

Structure of wire carpet films: Figure 1a displays an STM topograph with a closed monolayer EuCot wire carpet together with second layer EuCot wire islands on Gr/Ir(110). The length of the EuCot wires in the closed monolayer is insensitive to the preparation conditions and always exceeds the width of the topograph shown here, i.e. hundred unit cells. This likely holds as well for complete higher layers. In the inset of Figure 1a a ball model of the interlocking wires and the unit cell (green rhomboid) are overlaid on a molecular resolution topograph. The wire orientation along the [001] direction is imposed by the anisotropic moiré of Gr on Ir(110) as discussed in ref. 42. This uniaxial orientation is maintained in the second layer. STM topographs of thicker EuCot wire carpet films could not be obtained due to the poor conductivity of the film, resulting in tip-induced film changes.

However, LEED patterns prove that the uniaxial wire orientation along the [001] direction is maintained beyond the second layer. A LEED pattern of an ≈ 5 ML thick EuCot wire film is displayed in Figure 1b. Though not very shap, first order reflections of the EuCot wire carpet film are clearly present, while the Gr and Ir(110) substrate reflections are absent in consequence of the substantial EuCot film thickness. The reciprocal lattice vectors \vec{b}_1 and \vec{b}_2 for the EuCot layer are indicated by black arrows, and the first Brillouin zone of the EuCot layer is indicated in blue.

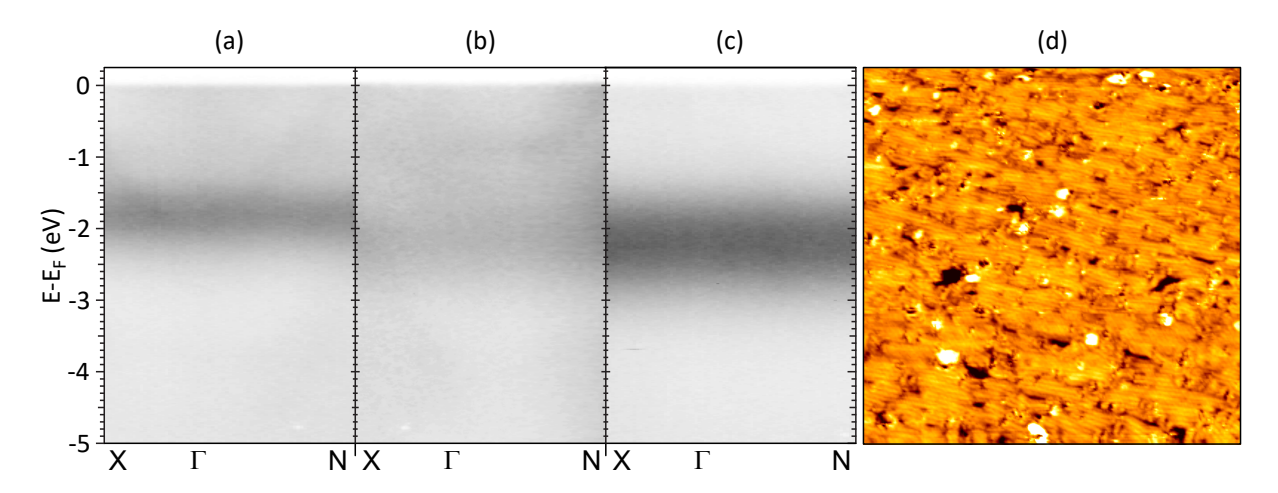


Figure 2: (a) Angle-resolved photo emission spectrum along $X-\Gamma-N$ for a 1 ML EuCot film recorded at a photon energy of 110 eV. The photon beam is moved over the sample limiting the photon dose at each location to $\approx 6 \cdot 10^3 \frac{\text{ph}}{\text{nm}^2}$. A flat band is visible at $-1.85 \, \text{eV}$. (b) ARPES spectrum along $X-\Gamma-N$ for a 1 ML EuCot film recorded at a photon energy of 100 eV. The flat band appears more blurred and is located in energy $-2.25 \, \text{eV}$. The photon beam is not moved over the sample and the integrated photon dose at the measurement location is $\approx 3 \cdot 10^5 \frac{\text{ph}}{\text{nm}^2}$. (c) ARPES spectrum along $X-\Gamma-N$ for a 4 ML EuCot film recorded at a photon energy of 100 eV. The flat band is pronounced and located in energy also at $-2.25 \, \text{eV}$. The photon beam is not moved over the sample and the integrated photon dose at the measurement location is $\approx 1.2 \cdot 10^7 \frac{\text{ph}}{\text{nm}^2}$. (d) STM topograph (500 × 500 Ų) of a 1 ML thick EuCot wire carpet after a photon dose of $\approx 6 \cdot 10^3 \frac{\text{ph}}{\text{nm}^2}$ in each sample location. Tunneling parameters are $U_{\text{bias}} = -2.12 \, \text{V}$ and $I_{\text{t}} = 0.14 \, \text{nA}$.

ARPES measurements of wire carpet films: ARPES measurements of globally aligned wire carpet films were conducted with the goal to measure the band structure of the wire carpet islands. Specifically along the wire axis, i.e. along the $\Gamma - N$ direction, dispersion could be expected. Figure 2a displays the measured band structure for a 1 ML

thick EuCot film along the wires in $\Gamma-N$ direction and normal to the wires in $\Gamma-X$ direction. The spectrum displays a single and flat band at $-1.85\,\mathrm{eV}$ with a full width at half maximum (FWHM) of $(1.0\pm0.2)\,\mathrm{eV}$. The entire $E(\vec{k})$ slice represented in Figure 2a is composed of ≈ 30 energy-scans, each at fixed polar angle θ . In order to minimize the effects of radiation damage, after each scan the beam (dimension $190\times90\,\mathrm{\mu m^2}$) was moved to a fresh, non-illuminated sample position. The photon dose at each location is $\approx 6\cdot10^3\,\frac{\mathrm{ph}}{\mathrm{nm^2}}$. When the photon beam is not moved over the sample surface, but resides in the same location for an extended measurement, the situation changes. Figure 2b displays the same $E(\vec{k})$ slice for a sample of the same EuCot film thickness as shown in Figure 2a, but without scanning and with an integrated photon dose larger by a factor of 50 at the location of measurement. The flat band is shifted down in energy to $-2.25\,\mathrm{eV}$ and appears blurred. For a thicker 4 ML EuCot film without scanning of the beam the $E(\vec{k})$ slice is represented in Figure 2c. The dispersionless band becomes more pronounced and remains at $-2.25\,\mathrm{eV}$. The FWHM of $(1.5\pm0.3)\,\mathrm{eV}$ is increased compared Figure 2a. The integrated photon dose at the location of photoemission is larger by factor of 2000 compared to Figure 2a.

Figure 2d displays an STM topograph of a sample where by moving the illuminating photon beam over the entire sample, to good approximation each location has been subject to a photon dose of $\approx 6 \cdot 10^3 \frac{\text{ph}}{\text{nm}^2}$. Clear signs of degradation of the EuCot carpet are already visible, namely dark holes and bright spots that are present in larger concentration than prior to illumination with photons (compare Figure 1a). Still in most areas the wires are intact, but display a shorter length due to the defects. We tentatively conclude that the ARPES slice represented in Figure 2a is from a marginally damaged still 'close to intact' EuCot film as represented by Figure 2d, while the downshift and broadening of the flat band as found for much larger photon doses in Figures 2b and 2c are attributed to radiation damage effects. This topic will be analyzed in more detail in the discussion.

Electronic structure calculations compared to experiments: To understand the origin of the flat band, we conducted DFT calculations and additional XPS measurements.

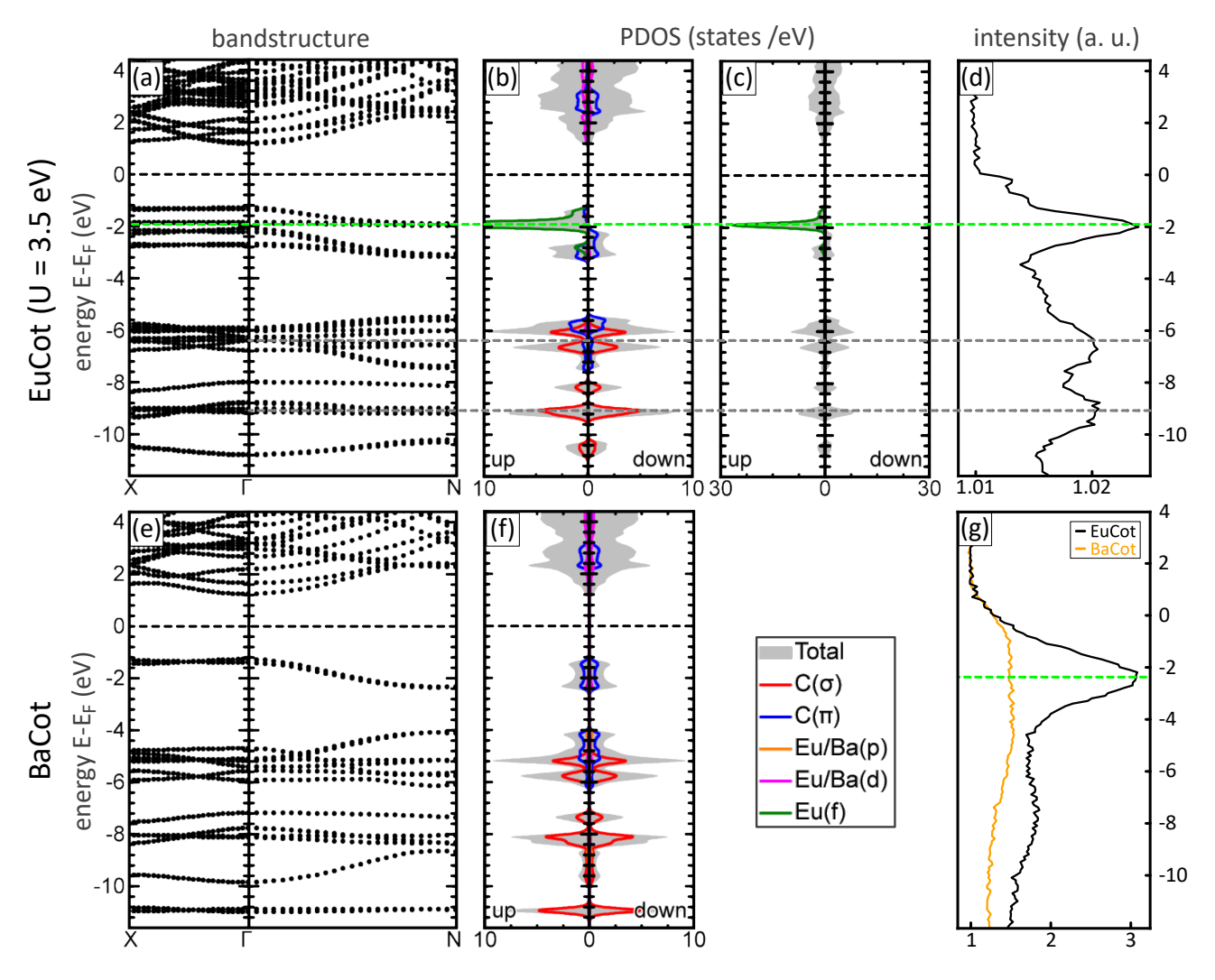


Figure 3: EuCot ML: (a) DFT band structure of 1 ML EuCot film along $X - \Gamma - N$. (b) Spin-polarized PDOS. (c) Larger scale spin-polarized PDOS. (d) Angle-integrated ARPES data of a 4 ML EuCot film. Position of 4f-derived peak is indicated by dotted green line in (a)-(d). (e) DFT band structure of 1 ML BaCot film along $X - \Gamma - N$. (f) Spin-polarized PDOS. (g) XPS data of EuCot (black) and BaCot (orange) multilayer film with thickness of ≈ 10 ML. The position of the 4f-derived peak is indicated by dotted green line. An effective Hubbard U of 3.5 eV (U = 4.4 eV and J = 0.9 eV) was used in the calculations. ARPES data were obtained at a photon energy $E_{\rm h\nu} = 130$ eV at T = 35 K. XPS data were obtained at a photon energy $E_{\rm h\nu} = 1486.6$ eV (Al K- α) at T = 300 K. Photon exposure for (d) is $\approx 6 \cdot 10^4 \frac{\rm ph}{\rm nm^2}$ at a photon energy of 130 eV.

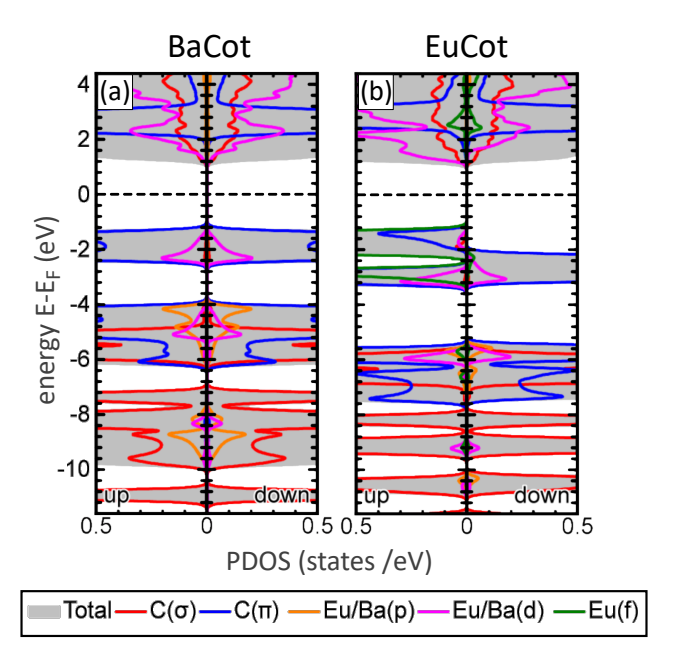


Figure 4: Detailed plot of spin-polarized PDOS (a) BaCot and (b) EuCot monolayers. Projections of the total DOS (shaded grey) onto the specified bands of C, Eu, and Ba are indicated in the legend. An effective Hubbard U of $3.5 \,\text{eV}$ ($U = 4.4 \,\text{eV}$ and $J = 0.9 \,\text{eV}$) to describe the Eu 4f states was used in the calculations.

The calculated band structure for a 1 ML EuCot carpet is shown in Figure 3a along $X-\Gamma-N$. Comparison with Figure 3b makes obvious that in the occupied states between $-3\,\mathrm{eV}$ and $-1.5\,\mathrm{eV}$ an Eu 4f-derived band without dispersion and carbon π bands with weak dispersion along $\Gamma-N$ are present. The absence of dispersion for the 4f-derived band at $-1.85\,\mathrm{eV}$ is consistent with the rather localized nature of the 4f wave functions, which are close to the Eu nucleus (see below for discussion of hybridization effects). In the larger scale representation of the PDOS in Figure 3c it is apparent that the 4f-derived peak at $-1.85\,\mathrm{eV}$ dominates the DOS and should give rise to the strongest signal in the experiment. Figure 3d shows the angle-integrated ARPES data of the 1 ML EuCot film with a strong peak at $-1.9\,\mathrm{eV}$, which is in correspondence with the flat band at $-1.85\,\mathrm{eV}$ of the ARPES data shown in Figure 2a. It can be attributed to the 4f states shown in the PDOS, as highlighted by the green dotted line. Also the two lower lying peaks of the angle integrated ARPES data shown in Figure 3d centered at $-6.4\,\mathrm{eV}$ and $-8.9\,\mathrm{eV}$ agree with the position of the π and σ states in the PDOS as highlighted by the grey dotted lines.

The set of three peaks in the angle-integrated ARPES data at $-1.9 \,\mathrm{eV}$, $-6.4 \,\mathrm{eV}$ and $-8.9 \,\mathrm{eV}$ was used to map out the proper choice of the Hubbard U, which was systematically varied from $3.5 \,\mathrm{eV}$ to $8.2 \,\mathrm{eV}$ (compare Figure S1 of the SI). The value of $U = 3.5 \,\mathrm{eV}$ of the calculated PDOS agrees best with the experimentally observed peaks.

In Figure 3e, we show the calculated band structure for a 1 ML BaCot wire carpet films, which looks similar to the one for EuCot (STM and LEED of BaCot wire carpets on Gr/Ir(111) can be found in Figure S2 of the SI). In the corresponding PDOS in Figure 3f the 4f-derived peak is missing, while the π and σ states are just slightly shifted in energy. Further, we also measured XP spectra on 10 ML EuCot and BaCot films shown in Figure 3g. For the EuCot spectrum (black line) we observe a large peak at $-2.2\,\mathrm{eV}$, while this peak is missing in the BaCot spectrum, which is is clear evidence that the flat band in ARPES at energies between $-1.85\,\mathrm{eV}$ and $-2.25\,\mathrm{eV}$ is derived from the Eu 4f states.

Hybrid electronic states and energetic position of 4f-derived band: The electronic configuration of Ba (5p⁶ 4f⁰ 5d⁰ 6s²) and Eu (5p⁶ 4f⁷ 5d⁰ 6s²) differs only in the occupation of 4f states. While the 4f shell is empty in Ba, it is half filled for Eu. Therefore, by comparison of the binding in EuCot and BaCot wires an insight into the effect of the 4f orbitals on the electronic structure and related energetic levels is gained.

In a simplified chemical picture, when Ba and Eu atoms interact with the cyclooctatetraene (C₈H₈, Cot) molecules, the two 6s electrons are transferred to the organic ligand. As a consequence, the binding within the BaCot and EuCot wires can be described as being of electrostatic nature and within this standard ionic picture a formal oxidation state of "2+" is expected for the metal atoms (i. e. Ba²⁺, Eu²⁺) and "2-" for the organic ligand (i.e. Cot²⁻). For an Eu²⁺ ion, one would expect the electrons in the 4f⁷ channel to localize closer to the atomic core and therefore to lie at lower energies (as compared to charge-neutral Eu atoms) and be purely atomic-like.

However, our theoretical simulations performed on BaCot and EuCot monolayers demonstrate that the specific chemical environment introduced by the π -electron cloud of the Cot

ligands around the metallic atoms changes the Ba and Eu valence electronic configurations. The binding is not purely of electrostatic nature but contains also a hybridization component between the π -electron cloud and the metal orbitals. This hybridization results in an uplift of the energetic position of the 4f states, as outlined below.

Figure 4 shows a magnified view of the spin-polarized PDOS for BaCot and EuCot ML films. As apparent from Figure 4a, for the BaCot ML film in both spin-channels the hybrid electronic states at about $-2\,\mathrm{eV}$ are dominated by the carbon π -like orbitals (blue), but also include a small contribution of Ba 5d states (cyan). Similarly, also for the EuCot ML film in the spin-down channel the hybrid electronic states at $\approx -3\,\mathrm{eV}$ are dominated by the carbon π -like orbitals (blue), but with a small contribution of Eu 5d states (cyan, compare Figure 4b). In the spin-up channel, additionally Eu 4f states (green) are energetically aligned with these EuCot hybrid electronic states, i.e. some hybrid states have a large 4f and small π contribution while other hybrid states have a larger π and smaller 5d and 4f character.

The projection of the total charge density in a sphere around the metal atom onto the s, p, d and f atomic-like orbitals leads to the following electronic occupation numbers: 0.08 in s, 5.64 in p, 0.43 in d and 0.00 in f for Ba and 0.04 in s, 5.85 in p, 0.44 in d and 6.88 in f for Eu, respectively. The magnetic moment per atom is 0.00 $\mu_{\rm B}$ for Ba and 6.95 $\mu_{\rm B}$ for Eu atoms (5p: -0.01 $\mu_{\rm B}$, 6s: +0.01 $\mu_{\rm B}$, 5d: +0.07 $\mu_{\rm B}$ and 4f: 6.88 $\mu_{\rm B}$).

Thus, the partial occupancies together with the energetic alignment of π , 5d, and 4f states indicate that in addition to the electrostatic interaction a hybridization occurs between Cot and Ba as well as between Cot and Eu. For Ba it is due to the overlap of the Cot π orbitals and Ba 5d states that have long tails extending further away from the metal ion. For Eu this hybridization is mediated through atomic hybrid orbitals with mixed 5d and 4f character rather than pure 5d character as for Ba. In other words, around the Eu atom, the local chemical environment provided by the Cot ligand is modified so that the atomic 5d and 4f states are allowed to mix while this is forbidden for an isolated atom. These atomic-like d–f states have a large 4f atomic character close to the nucleus and long tails extending further

away from the nucleus, originating from the Eu 5d atomic-like orbitals. As a consequence of the long spatial extent, these Eu atomic-like d–f orbitals can overlap and hybridize with the Cot π orbitals. Thus the flat band visible in ARPES does not represent entirely localized 4f states, but electrons able to hop along the wire due to hybridization effects.

XAS measurements: To further access the electronic and magnetic properties of EuCot nanowires on Gr/Ir(110), XAS and XMCD data have been measured at the Eu M_{5,4} edges, probing the properties of the 4f states. Figure 5a displays the averaged XAS of the Eu $M_{5,4}$ edges measured at the grazing incidence of $\theta = 60^{\circ}$. Comparison of the spectral shape to literature data 66 and multiplet calculations prove a $4f^7$ electronic configuration of the Eu in the EuCot nanowires. The spectrum is nearly identical to the one obtained from EuCot wire carpet islands grown on Gr/Ir(111).⁴¹ The normalized XMCD signal in Figure 5b provides information about the magnetic moment of the Eu. By applying sum-rule analysis 67,68 the spin and orbital magnetic moment of the Eu can be extracted. Here, we obtain a spin moment of $\mu_{\rm S}=(7.2\pm0.6)\mu_{\rm B}$ and orbital moment of $\mu_{\rm L}=(0.0\pm0.4)\mu_{\rm B}$. The dipolar term <T_z> is approximated to be zero, based on the half-filled 4f shell. $^{68-70}$ The resulting moments are in good agreement with the expectation for atomic Eu with $\mu_{\rm S}=7\,\mu_{\rm B}$ and $\mu_{\rm L}=0\,\mu_{\rm B}$ and the results for EuCot wire carpets adsorbed on Gr/Ir(111) in ref. 41. The spin and orbital moments measured at normal incidence ($\theta = 0^{\circ}$) are $\mu_{\rm S} = (7.0 \pm 0.8) \mu_{\rm B}$ and $\mu_{\rm L} = (0.1 \pm 0.4) \mu_{\rm B}$. They agree with the moments obtained for grazing incidence within the limits of error. The corresponding spectra are shown in Figure S3 of the SI.

Figure 5c displays the field-dependent XMCD signal at the M_5 edge normalized to the pre-edge, which is proportional to the magnetic moment. For a better overview, the up and down branches of each orientation are averaged. The magnetization curves of EuCot nanowires on Gr/Ir(110) are measured for normal ($\theta=0$ °) and grazing ($\theta=60$ °) incidence at T=3K. Saturation is reached at $\approx 4T$ for both orientations. In the following we compare the slopes around zero field (compare Figure S4 of the SI) which are proportional to the zero field susceptibilities χ , since $\langle T_z \rangle = 0$ and both curves reach the same saturation

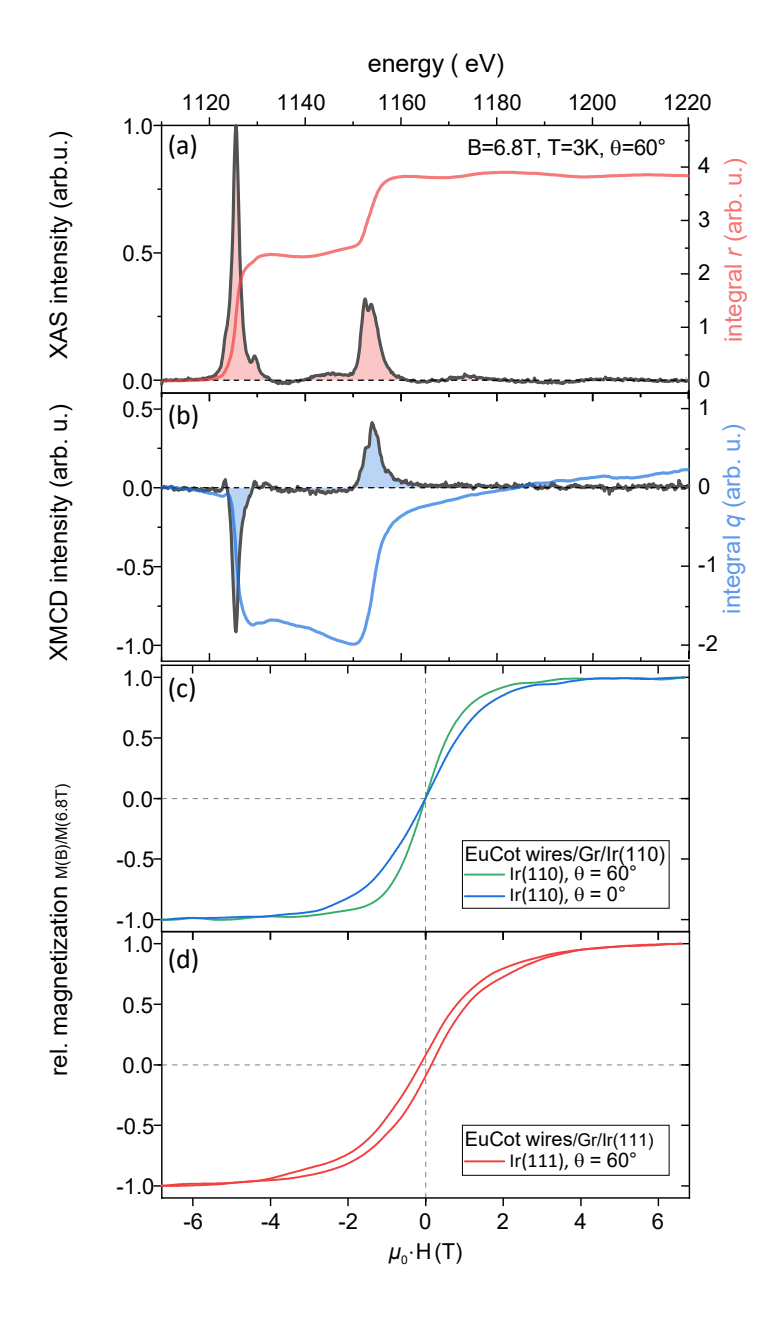


Figure 5: (a) Average XAS $\frac{1}{2}(\mu_+ + \mu_-)$ of the Eu M₅ and M₄ edges measured at grazing incidence $\theta = 60$ ° off surface normal tilted into the [001] direction, T = 3 K, and B = 6.8 T (grey line). The red line represents the integral over the averaged XAS. (b) Normalized XMCD ($\mu_+ - \mu_-$) (black line) and its integral (blue line). (c) Averaged and smoothed magnetization curves based on the field dependent XMCD signal of the Eu M₅ edge for grazing and normal incidence at T = 3 K. Grazing incidence is along the [001] direction, i.e. along the wire axis. (d) Comparison to the averaged and smoothed XMCD magnetization curves of EuCot nanowires/Gr/Ir(111) at grazing incidence and T = 3 K.

magnetization within the limits of error. The susceptibility for grazing incidence along the [001] direction is $\chi_{60^{\circ}-[001]} = \alpha \cdot (1.01 \pm 0.08) \,\mathrm{T}^{-1}$ which is larger by a factor of 1.6 compared to the one at normal incidence of $\chi_{0^{\circ}} = \alpha \cdot (0.64 \pm 0.06) \,\mathrm{T}^{-1}$. Here, α is the proportionality constant between the measured slopes and the susceptibility. In comparison, the susceptibility $\chi_{60^{\circ}-[1\bar{1}0]}$ measured at grazing incidence along the [1 $\bar{1}0$] direction — i.e. normal to the wire axis — is close to $\chi_{0^{\circ}}$, only larger by a factor of 1.2. Thus the easy axis of magnetization is along the [001] direction.

Neither for grazing nor for normal X-ray incidence the magnetization curves for EuCot wire carpets on Gr/Ir(110) in Figure 5c display a hysteresis. This is surprising in view of the fact that for EuCot/Gr/Ir(111) represented by Figure 5d hysteresis is found at grazing incidence. The EuCot/Gr/Ir(111) data shown were measured subsequently with the same set-up under the same conditions as the EuCot/Gr/Ir(110) data. The data for EuCot/Gr/Ir(111) in Figure 5d agree well with the results of ref. 41. In previous work we established that through radiation damage, the hysteresis loop for EuCot wire carpets on Gr/Ir(111) disappears and additional changes in the spectral shape of the XAS take place, which are absent here. Therefore, the observed hysteresis in the EuCot wire carpet on Gr/Ir(111) indicates the absence of significant radiation damage during XAS in the present measurements for both substrates.

Discussion: One of the goals of this work was to measure the band structure of the EuCot wires. Band structure measurements of 1D organometallic systems have not been conducted before and our measurements provide evidence that the determination of band structures of organometallic films built from 1D objects is demanding. Organometallic 1D wires seem to be more sensitive to photon irradiation than organic crystals, which display some radiation damage, ⁴⁶ much more sensitive than π -conjugated covalently-bonded 1D polymers, for which no radiation damage was reported. ^{47–50} The sensitivity to radiation damage is also obvious from LEED: a LEED pattern taken with a conventional LEED setup, rather than with a microchannel plate-LEED, fades away within a minute. The STM and

ARPES data shown in Figure 2 document a fluence-dependent damage under photoemission conditions. It is thus obvious that low-energy electrons in the energy range at and below 100 eV cause radiation damage. Whether this is the exclusive effect or whether also X-rays themselves cause damage cannot be answered on the basis of the present data. STM data after scanning the sample with a photon fluence $\approx 6 \cdot 10^3 \frac{\text{ph}}{\text{nm}^2}$ exhibit already first signs of damage. However, extended wire segments are still visible and therefore we are convinced that the spectrum displayed in Figure 2a is still close to a situation without radiation damage. In any case, scanning the X-ray beam over the sample turned out to be an effective tool to limit radiation damage.

There is no single obvious explanation for the downshift and broadening of the 4f-derived flat band due to radiation damage. We speculate that decomposition of EuCot leads to the formation of metallic Eu, which is known to locally n-dope Gr, i.e. to locally move the Fermi level in Gr up (or its work function down). This would imply a corresponding shift of the Fermi level within the semiconducting EuCot wires. Because of the low density of states in Gr, one donated electron per 200 C atoms would be sufficient to explain the observed Fermi level shift of about $0.4 \, \mathrm{eV}$, a number that seems to be compatible with the defect pattern visible in the STM topograph of Figure 2d. The local variation of the doping level would then give a simple explanation for the observed broadening of the 4f-derived band.

The position of the 4f-drived band about -1.85 eV below the Fermi level is within the range of what has been found for Eu metal⁷³ and Eu oxide systems.⁷⁴ One of the nice features of our experiments is the experimental determination of the proper Hubbard U to be used in organometallic compounds with Eu. Tuning the relative position of the 4f-derived peak and the lower-lying peaks of the PDOS to the ARPES data through varying the value of U (shown in Figure S1 in the SI) is a straightforward way to access the magnitude of this quantity, which is otherwise difficult to obtain. Our best match to the experimental data with $U = 3.5 \,\mathrm{eV}$ justifies in retrospect the use of $U = 3.7 \,\mathrm{eV}$ in previous DFT calculations for EuCot wires, ^{35-37,39} where this value was picked without explicated reasoning. It should

also be noted here that the detailed PDOS in Figure 4b shows a slight hybridization of the Eu 4f states with the Eu 5d and the carbon π states, aligning their positions and giving rise to the band character with electron hopping.

The absence of dispersing π -derived bands in our ARPES data can be rationalized simply by considering the relative weights of the different states in the PDOS as presented in Figure 3b and 3c. The 4f-derived peak in the PDOS is about a factor 30 higher than any peak related to π states within the energy range investigated by ARPES. Therefore, the lack of a dispersing π -derived band could simply be due to a too large intensity of the 4f-derived band next to it.

One strategy to avoid this intensity problem and to obtain at least some information could be to conduct ARPES for BaCot instead of EuCot. The 4f-derived band is missing for BaCot and π -derived bands might become detectable. However, the π -derived bands are similar according to our DFT calculations (compare Figure 3a and c), but not identical.

Moreover, a close inspection of Figure 2a reveals that the flat 4f band has only a 3 to 4 times higher intensity than the background. Thus even if the 4f-derived band at -1.85 eV would be missing, a π -derived band with a 30 times weaker intensity would create a signal hardly outside the noise level of the background. A careful evaluation of polarization-dependent matrix elements for the π system together with the experimental possibility to change the polarization conditions, ideally with the option to change both the light polarization and the angle of incidence, could improve this intensity ratio to some degree.

EuCot wire carpets on Gr/Ir(111) were shown to be ferromagnetic insulators with a Curie temperature between 5 K and 7 K, i.e. the magnetization loop is open at 5 K, but already closed at 7 K.⁴¹ On Gr/Ir(111) the EuCot carpet islands form in close-to-random orientation, averaging out any in-plane anisotropy and reducing the maximum susceptibility. Therefore, one expects for a globally aligned EuCot wire carpet film an (i) increased susceptibility when the projection of magnetic field onto the surface is along the easy axis and (ii) consequently for the same orientation of the magnetic field also a larger hysteresis of the magnetization

as compared to a film of randomly oriented EuCot wire carpet islands.

In the experiment we indeed find that with respect to (i) the measured susceptibility becomes anisotropic in-plane. While the susceptibility $\chi_{60^{\circ}-[1\bar{1}0]}$ is close to $\chi_{0^{\circ}}$, $\chi_{60^{\circ}-[001]}$ is larger by a factor of ≈ 1.6 . This is clear evidence for an easy magnetic axis along the wire, as it would for instance be favored by dipolar interactions.⁴¹

With respect to our expectation (ii) we do not find a larger hysteresis. To the contrary, the hysteresis vanishes as shown in Figure 5 and only paramagnetic behavior is observed at 3 K. However, the change is subtle: On Gr/Ir(111) the magnetization loop is closed at 7 K while on Gr/Ir(110) it is closed at 3 K, i.e. the change in Curie temperature is no more than a few Kelvin.

Evidently, the suppression of the magnetic hysteresis is caused by a slightly modified interaction between the wire carpet and the substrate. While our DFT calculations neglecting a substrate capture the essential features of the wire carpet electronic structure, comparative DFT calculations of the wire carpet resting either on Gr/Ir(110) or Gr/Ir(111) could provide insight into the origin of the changes in the magnetic structure. But to obtain a reasonable approximation of the physical situation, the mismatch of the wire carpet with the already large moiré supercell of Gr/Ir(110) would require an even larger DFT supercell beyond the limits of efficient computation.

Therefore we can only speculate here about the differences in the interaction of the two substrates with EuCot wires giving rise to the modified magnetic behavior. In order to avoid misunderstandings, we point out that also Gr on Ir(110) is an inert substrate, similar to Gr on Ir(111).⁴² To both substrates aromatic molecules were only found to bind through van der Waals interactions without charge transfer.^{42,63} Since the Cot molecules are standing upright on Gr with the outermost H atoms forming already a bond to the C atoms of the Cot, these atoms cannot chemically interact with the Gr substrate. Thus the EuCot wires are only physisorbed to Gr on the two differently oriented Ir substrates.

An obvious difference between the two substrates is their different Gr density of states near

the Fermi level, which is marginal for Gr/Ir(111)? and substantial for Gr/Ir(110) due to Gr's hybridization with Ir.⁴² The binding within EuCot wires is largely of ionic type, between positively charged Eu²⁺ and negatively charged Cot²⁻ ions. A variation of the density of states in Gr around the Fermi level modifies the screening of the electrostatic interactions between the wire anions and cations through the Gr electrons. Thus the binding strength within the EuCot wire is affected, which will slightly modify binding distances and in turn may modify the magnetic coupling of Eu ions through the Cot molecules.

Based on this argument, one might speculate that electronically intact, but strongly n-doped or p-doped 'metallic' Gr, could suppress the open magnetization loop in a similar way as found on Gr/Ir(110). Indeed, when Gr/Ir(111) is intercalated by Yb, a strong n-dopant for Gr due to its two 6s electrons, the open magnetization curve is also suppressed (compare Figure S5 in the SI). Still this reasoning remains speculative and other effects not considered here could be of relevance.

Conclusion

Uniaxial alignment of EuCot wires on Gr along the [001] direction of the Ir(110) substrate is imposed by the Gr moiré and persists from submonolayer islands up to multilayer films. This alignment provides access to the structural, electronic, and magnetic properties of such wire systems using spatially-averaging techniques.

Contrary to expectation, ARPES could not detect dispersing π -derived bands, but only a flat band 1.85 eV below the Fermi energy. Using complementary DFT calculations and XPS measurements we attribute this flat band to be derived from Eu 4f states. By comparing the position of the 4f states with the lower-lying σ bands we pinpoint the Hubbard U of this system to be close to $U=3.5\,\text{eV}$. A detailed PDOS analysis indicates hybridization of the π orbitals with f-d Eu hybrid orbitals, which effectively lifts the 4f-derived band up in energy. The absence of dispersing π -derived bands may be due to their much lower DOS, which in

combination with quick decomposition through radiation damage leaves them unobservable. Our results are yet another example that radiation damage must be carefully considered, when investigating organometallic systems with energetic electrons or photons.

For the magnetic properties of the oriented EuCot wire sample we find —consistent with EuCot/Gr/Ir(111)— that the Eu ion has [Xe]4f⁷ 6s⁰ configuration, resulting in a magnetic moment of $7 \mu_{\rm B}$. Magnetization close to the wire axis displays the highest susceptibility, making plain that the easy magnetization axis is along the wires. Magnetic hysteresis observed on Gr/Ir(111) vanishes for the EuCot wire carpet on Gr/Ir(110) 3 K. We speculate that enhanced screening for the more 'metallic' Gr/Ir(110) substrate affects the ionic binding of the wires which in turn might influence their subtle magnetic ordering.

Supporting Information Available

Figure S1: Comparison of EuCot ML theoretical bandstructure and DOS with angle-integrated ARPES data for different values of Hubbard U. Figure S2: STM topograph and LEED pattern of BaCot wire carpets on Gr/Ir(111). Figure S3: XAS and XMCD data of EuCot wires on Gr/Ir(110) at normal incidence. Figure S4: Magnetization curves of EuCot wires on Gr/Ir(110) at normal and grazing incidence with indicated slopes around zero field. Figure S5: Magnetization curve of EuCot wires on Gr/Yb/Ir(111) at grazing incidence.

Acknowledgement

This work was funded by the Deutsche Forschungsgemeinschaft (DFG, German Research Foundation) within the project 'Sandwich molecular nanowires: on-surface synthesis, structure and magnetism' (MI 581/23-1, AT 109/5-1 and WE 2623/17-1). V. C. and N. A. acknowledge additional DFG support within CRC1238, project no. 277146874 - CRC 1238 (subproject C01). We gratefully acknowledge the Gauss Centre for Supercomputing (GCS) for providing computing time through the John von Neumann Institute for Computing (NIC)

on the GCS share of the supercomputer JURECA at Jülich Supercomputing Centre (JSC). This work was also supported by VILLUM FONDEN via the Centre of Excellence for Dirac Materials (Grant No. 11744).

References

- (1) Sanvito, S. Molecular spintronics. Chem. Soc. Rev. 2011, 40, 3336–3355.
- (2) Rinehart, J. D.; Fang, M.; Evans, W. J.; Long, J. R. A N₂³⁻ radical-bridged terbium complex exhibiting magnetic hysteresis at 14 K. J. Am. Chem. Soc. **2011**, 133, 14236–14239.
- (3) Westerström, R.; Uldry, A.-C.; Stania, R.; Dreiser, J.; Piamonteze, C.; Muntwiler, M.; Matsui, F.; Rusponi, S.; Brune, H.; Yang, S.; Popov, A.; Büchner, B.; Delley, B.; Greber, T. Surface aligned magnetic moments and hysteresis of an endohedral single-molecule magnet on a metal. *Phys. Rev. Lett.* 2015, 114, 087201.
- (4) Wäckerlin, C.; Donati, F.; Singha, A.; Baltic, R.; Rusponi, S.; Diller, K.; Patthey, F.; Pivetta, M.; Lan, Y.; Klyatskaya, S.; Ruben, M.; Brune, H.; Dreiser, J. Giant hysteresis of single-molecule magnets adsorbed on a nonmagnetic insulator. Adv. Mater. 2016, 28, 5195-5199.
- (5) Baltic, R.; Donati, F.; Singha, A.; Wäckerlin, C.; Dreiser, J.; Delley, B.; Pivetta, M.; Rusponi, S.; Brune, H. Magnetic properties of single rare-earth atoms on graphene/Ir(111). Phys. Rev. B 2018, 98, 024412.
- (6) Diller, K.; Singha, A.; Pivetta, M.; Wäckerlin, C.; Hellwig, R.; Verdini, A.; Cossaro, A.; Floreano, L.; Vélez-Fort, E.; Dreiser, J.; Rusponi, S.; Brune, H. Magnetic properties of on-surface synthesized single-ion molecular magnets. RSC Adv. 2019, 9, 34421–34429.
- (7) Donati, F.; Rusponi, S.; Stepanow, S.; Persichetti, L.; Singha, A.; Juraschek, D. M.;

- Wäckerlin, C.; Baltic, R.; Pivetta, M.; Diller, K.; Nistor, C.; Dreiser, J.; Kummer, K.; Velez-Fort, E.; Spaldin, N. A.; Brune, H.; Gambardella, P. Unconventional spin relaxation involving localized vibrational modes in Ho single-atom magnets. *Phys. Rev. Lett.* **2020**, *124*, 077204.
- (8) Serrano, G.; Poggini, L.; Briganti, M.; Sorrentino, A. L.; Cucinotta, G.; Malavolti, L.; Cortigiani, B.; Otero, E.; Sainctavit, P.; Loth, S.; Parenti, F.; Barra, A.-L.; Vindigni, A.; Cornia, A.; Totti, F.; Mannini, M.; Sessoli, R. Quantum dynamics of a single molecule magnet on superconducting Pb(111). Nat. Mater. 2020, 19, 546-551.
- (9) Chen, C.-H.; Spree, L.; Koutsouflakis, E.; Krylov, D. S.; Liu, F.; Brandenburg, A.; Velkos, G.; Schimmel, S.; Avdoshenko, S. M.; Fedorov, A.; Weschke, E.; Choueikani, F.; Ohresser, P.; Dreiser, J.; Büchner, B.; Popov, A. A. Magnetic hysteresis at 10 K in single molecule magnet self-assembled on gold. Adv. Sci. 2021, 8, 2000777.
- (10) Dreiser, J.; Wäckerlin, C.; Buzzi, M.; Pedersen, K. S.; Bendix, J. Island formation of Er(trensal) single-ion magnets on graphene observed on the micrometer scale. RSC Adv. 2021, 11, 9421–9425.
- (11) Stepanow, S.; Lin, N.; Payer, D.; Schlickum, U.; Klappenberger, F.; Zoppellaro, G.; Ruben, M.; Brune, H.; Barth, J.; Kern, K. Surface-assisted assembly of 2D metal-organic networks that exhibit unusual threefold coordination symmetry. Angew. Chem. Int. Ed. 2007, 46, 710-713.
- (12) Vijayaraghavan, S.; Ecija, D.; Auwärter, W.; Joshi, S.; Seufert, K.; Drach, M.; Nieckarz, D.; Szabelski, P.; Aurisicchio, C.; Bonifazi, D.; Barth, J. V. Supramolecular assembly of interfacial nanoporous networks with simultaneous expression of metal-organic and organic-bonding motifs. *Chem. Eur. J.* **2013**, *19*, 14143–14150.
- (13) Urgel, J. I.; Cirera, B.; Wang, Y.; Auwärter, W.; Otero, R.; Gallego, J. M.; Alcamí, M.; Klyatskaya, S.; Ruben, M.; Martín, F.; Miranda, R.; Ecija, D.; Barth, J. V. Surface-

- supported robust 2D lanthanide-carboxylate coordination networks. *Small* **2015**, *11*, 6358–6364.
- (14) Wäckerlin, C.; Ernst, K.-H. Autocatalytic surface explosion chemistry of 2D metalorganic frameworks. J. Phys. Chem. C 2021, 125, 13343–13349.
- (15) Yang, Z.; Lotze, C.; Franke, K. J.; Pascual, J. I. Metal-organic superlattices induced by long-range repulsive interactions on a metal surface. *J. Phys. Chem. C* **2021**, *125*, 18494–18500.
- (16) Umbach, T. R.; Bernien, M.; Hermanns, C. F.; Krüger, A.; Sessi, V.; Fernandez-Torrente, I.; Stoll, P.; Pascual, J. I.; Franke, K. J.; Kuch, W. Ferromagnetic coupling of mononuclear Fe centers in a self-assembled metal-organic network on Au(111). Phys. Rev. Lett. 2012, 109, 267207.
- (17) Schouteden, K.; Ivanova, T.; Li, Z.; Iancu, V.; Janssens, E.; Van Haesendonck, C. Probing magnetism in 2D molecular networks after in situ metalation by transition metal atoms. J. Phys. Chem. Lett. 2015, 6, 1048–1052.
- (18) Pacchioni, G. E.; Pivetta, M.; Gragnaniello, L.; Donati, F.; Autès, G.; Yazyev, O. V.; Rusponi, S.; Brune, H. Two-orbital kondo screening in a self-assembled metal-organic complex. ACS Nano 2017, 11, 2675–2681.
- (19) Blanco-Rey, M.; Sarasola, A.; Nistor, C.; Persichetti, L.; Stamm, C.; Piamonteze, C.; Gambardella, P.; Stepanow, S.; Otrokov, M. M.; Golovach, V. N.; Arnau, A. Magnetic properties of metal-organic coordination networks based on 3d transition metal atoms. *Molecules* 2018, 23.
- (20) Schulz, S.; Nechaev, I. A.; Güttler, M.; Poelchen, G.; Generalov, A.; Danzenbächer, S.; Chikina, A.; Seiro, S.; Kliemt, K.; Vyazovskaya, A. Y.; Kim, T. K.; Dudin, P.; Chulkov, E. V.; Laubschat, C.; Krasovskii, E. E.; Geibel, C.; Krellner, C.; Kummer, K.;

- Vyalikh, D. V. Emerging 2D-ferromagnetism and strong spin-orbit coupling at the surface of valence-fluctuating EuIr₂Si₂. npj Quantum Mater. **2019**, 4, 26.
- (21) Wang, L.; Cai, Z.; Wang, J.; Lu, J.; Luo, G.; Lai, L.; Zhou, J.; Qin, R.; Gao, Z.; Yu, D.; Li, G.; Mei, W. N.; Sanvito, S. Novel one-dimensional organometallic half metals: vanadium-cyclopentadienyl, vanadium-cyclopentadienyl-benzene, and vanadium-anthracene wires. *Nano Lett.* **2008**, *8*, 3640–3644.
- (22) Zhang, X.; Cao, M.; Liu, L.; Liu, Y. Tunable electronic and magnetic properties of boron/nitrogen-doped BzTMCp*TMBz/CpTMCp*TMCp clusters and one-dimensional infinite molecular wires. J. Phys. Chem. C 2014, 118, 11620–11627.
- (23) Lu, K.; Gao, W.; Xu, M.; Sun, Y.; Li, J.; Yao, X.; Liu, Y.; Zhang, X. Spin Transport Properties of One-Dimensional Benzene Ligand Organobimetallic Sandwich Molecular Wires. ACS Omega 2020, 5, 5534–5539.
- (24) Masubuchi, T.; Nakajima, A. Electronic Properties of Transition Metal-Benzene Sandwich Clusters. Springer 2020, 313–349.
- (25) Zhou, L.; Yang, S.-W.; Ng, M.-F.; Sullivan, M. B.; Tan,; Shen, L. One-dimensional iron-cyclopentadienyl sandwich molecular wire with half metallic, negative differential resistance and high-spin filter efficiency properties. J. Am. Chem. Soc. 2008, 130, 4023–4027.
- (26) Shen, L.; Yang, S.-W.; Ng, M.-F.; Ligatchev, V.; Zhou, L.; Feng, Y. Charge-transfer-based mechanism for half-metallicity and ferromagnetism in one-dimensional organometallic sandwich molecular wires. J. Am. Chem. Soc. 2008, 130, 13956–13960.
- (27) Li, Y.; Zhou, G.; Li, J.; Wu, J.; Gu, B.-L.; Duan, W. *Ab initio* study of half-metallicity and magnetism of complex organometallic molecular wires. *J. Phys. Chem. C* **2011**, 115, 7292–7297.

- (28) Joshi, M.; Ghanty, T. K. Prediction of a nine-membered aromatic heterocyclic 1,4,7-triazacyclononatetraenyl anion and its sandwich complexes with divalent lanthanides.

 ChemistrySelect 2019, 4, 9940–9946.
- (29) Zhang, X.; Gong, X.; Sun, Y.; Xu, M.; Xi, B.; Zhao, X.; Ye, X.; Yao, X.; He, M.; Liu, L.; Liu, Y. 3d transition metal-metallofullerene-ligand molecular wires: robust onedimensional antiferromagnetic semiconductors. J. Phys. Chem. C 2019, 123, 30571– 30577.
- (30) de Camargo, L. C.; Briganti, M.; Santana, F. S.; Stinghen, D.; Ribeiro, R. R.; Nunes, G. G.; Soares, J. F.; Salvadori, E.; Chiesa, M.; Benci, S.; Torre, R.; Sorace, L.; Totti, F.; Sessoli, R. Exploring the organometallic route to molecular spin qubits: the [CpTi(cot)] case. Angew. Chem. Int. Ed. 2021, 60, 2588-2593.
- (31) Kurikawa, T.; Negishi, Y.; Hayakawa, F.; Nagao, S.; Miyajima, K.; Nakajima, A.; Kaya, K. Multiple-decker sandwich complexes of lanthanide-1,3,5,7-cyclooctatetraene [Ln_n(C₈H₈)_m] (Ln = Ce, Nd, Eu, Ho, and Yb); localized ionic bonding structure. J. Am. Chem. Soc. 1998, 120, 11766-11772.
- (32) Hosoya, N.; Takegami, R.; Suzumura, J.-i.; Yada, K.; Koyasu, K.; Miyajima, K.; Mitsui, M.; Knickelbein, M. B.; Yabushita, S.; Nakajima, A. Lanthanide organometallic sandwich nanowires: formation mechanism. *J. Phys. Chem. A* **2005**, *109*, 9–12.
- (33) Miyajima, K.; Knickelbein, M. B.; Nakajima, A. Stern-Gerlach Study of Multidecker Lanthanide-Cyclooctatetraene Sandwich Clusters. J. Phys. Chem. A 2008, 112, 366– 375.
- (34) Hosoya, N.; Takegami, R.; Suzumura, J.-i.; Yada, K.; Miyajima, K.; Mitsui, M.; Knickelbein, M. B.; Yabushita, S.; Nakajima, A. Formation and electronic structures of organoeuropium sandwich nanowires. *J. Phys. Chem. A* **2014**, *118*, 8298–8308.

- (35) Atodiresei, N.; Dederichs, P. H.; Mokrousov, Y.; Bergqvist, L.; Bihlmayer, G.; Blügel, S. Controlling the magnetization direction in molecules via their oxidation state. *Phys. Rev. Lett.* **2008**, *100*, 117207.
- (36) Zhang, X.; Ng, M.-F.; Wang, Y.; Wang, J.; Yang, S.-W. Theoretical studies on structural, magnetic, and spintronic characteristics of sandwiched $\operatorname{Eu}_n\operatorname{COT}_{n+1}$ (n = 1-4) clusters. *ACS Nano* **2009**, 3, 2515–2522.
- (37) Xu, K.; Huang, J.; Lei, S.; Su, H.; Boey, F. Y. C.; Li, Q.; Yang, J. Efficient organometallic spin filter based on europium-cyclooctatetraene wire. *J. Chem. Phys.* **2009**, *131*, 104704.
- (38) Liu, X.; Tan, Y.; Zhang, G.; Pei, Y. Electronic structure and spin transport properties of a new class of semiconductor surface-confined one-dimensional half-metallic [Eu- (C_nH_{n-2})]_N (n = 7-9) sandwich compounds and molecular wires: first principle studies. J. Phys. Chem. C **2018**, 122, 16168–16177.
- (39) Yao, X.; Yuan, S.; Wang, J. Theoretical studies of sandwich molecular wires with europium and boratacyclooctatetraene ligand and the structure on a H-Ge(001)-2x1 surface. J. Phys. Chem. C 2016, 120, 7088-7093.
- (40) Huttmann, F.; Schleheck, N.; Atodiresei, N.; Michely, T. On-surface synthesis of sandwich molecular nanowires on graphene. J. Am. Chem. Soc. 2017, 139, 9895–9900.
- (41) Huttmann, F.; Rothenbach, N.; Kraus, S.; Ollefs, K.; Arruda, L. M.; Bernien, M.; Thonig, D.; Delin, A.; Fransson, J.; Kummer, K.; Brookes, N. B.; Eriksson, O.; Kuch, W.; Michely, T.; Wende, H. Europium cyclooctatetraene nanowire carpets: a low-dimensional, organometallic, and ferromagnetic insulator. J. Phys. Chem. Lett. 2019, 10, 911–917.
- (42) Kraus, S.; Huttmann, F.; Fischer, J.; Knispel, T.; Bischof, K.; Herman, A.; Bianchi, M.;

- Stan, R.-M.; Holt, A. J.; Caciuc, V.; Tsukamoto, S.; Wende, H.; Hofmann, P.; Atodiresei, N.; Michely, T. Single-crystal graphene on Ir(110). arXiv:2109.04198 2021,
- (43) Koller, G.; Berkebile, S.; Oehzelt, M.; Puschnig, P.; Ambrosch-Draxl, C.; Netzer, F. P.; Ramsey, M. G. Intra- and intermolecular band dispersion in an organic crystal. *Science* 2007, 317, 351–355.
- (44) Machida, S.-i.; Nakayama, Y.; Duhm, S.; Xin, Q.; Funakoshi, A.; Ogawa, N.; Kera, S.; Ueno, N.; Ishii, H. Highest-occupied-molecular-orbital band dispersion of rubrene single crystals as observed by angle-resolved ultraviolet photoelectron spectroscopy. *Phys. Rev.* Lett. 2010, 104, 156401.
- (45) Nitta, J.; Miwa, K.; Komiya, N.; Annese, E.; Fujii, J.; Ono, S.; Sakamoto, K. The actual electronic band structure of a rubrene single crystal. *Sci. Rep.* **2019**, *9*, 9645.
- (46) Nakayama, Y.; Kera, S.; Ueno, N. Photoelectron spectroscopy on single crystals of organic semiconductors: experimental electronic band structure for optoelectronic properties. J. Mater. Chem. C 2020, 8, 9090–9132.
- (47) Piquero-Zulaica, I.; Garcia-Lekue, A.; Colazzo, L.; Krug, C. K.; Mohammed, M. S. G.; Abd El-Fattah, Z. M.; Gottfried, J. M.; de Oteyza, D. G.; Ortega, J. E.; Lobo-Checa, J. Electronic structure tunability by periodic meta-ligand spacing in one-dimensional organic semiconductors. ACS Nano 2018, 12, 10537–10544.
- (48) Basagni, A.; Vasseur, G.; Pignedoli, C. A.; Vilas-Varela, M.; Peña, D.; Nicolas, L.; Vitali, L.; Lobo-Checa, J.; de Oteyza, D. G.; Sedona, F.; Casarin, M.; Ortega, J. E.; Sambi, M. Tunable band alignment with unperturbed carrier mobility of on-surface synthesized organic semiconducting wires. ACS Nano 2016, 10, 2644-2651.
- (49) García-Fernández, C.; Sierda, E.; Abadía, M.; Bugenhagen, B.; Prosenc, M. H.; Wiesendanger, R.; Bazarnik, M.; Ortega, J. E.; Brede, J.; Matito, E.; Arnau, A. Exploring the

- relation between intramolecular conjugation and band dispersion in one-dimensional polymers. J. Phys. Chem. C 2017, 121, 27118–27125.
- (50) Vasseur, G.; Fagot-Revurat, Y.; Sicot, M.; Kierren, B.; Moreau, L.; Malterre, D.; Cardenas, L.; Galeotti, G.; Lipton-Duffin, J.; Rosei, F.; Di Giovannantonio, M.; Contini, G.; Le Fèvre, P.; Bertran, F.; Liang, L.; Meunier, V.; Perepichka, D. F. Quasi one-dimensional band dispersion and surface metallization in long-range ordered polymeric wires. *Nature Commun.* **2016**, *7*, 10235.
- (51) van Gastel, R.; N'Diaye, A. T.; Wall, D.; Coraux, J.; Busse, C.; Buckanie, N. M.; Meyer zu Heringdorf, F.-J.; Horn von Hoegen, M.; Michely, T.; Poelsema, B. Selecting a single orientation for millimeter sized graphene sheets. Appl. Phys. Lett. 2009, 95, 121901.
- (52) Horcas, I.; Fernández, R.; Gómez-Rodríguez, J. M.; Colchero, J.; Gómez-Herrero, J.; Baro, A. M. WSXM: A software for scanning probe microscopy and a tool for nanotechnology. Rev. Sci. Instrum. 2007, 78, 013705.
- (53) Hoffmann, S. V.; Søndergaard, C.; Schultz, C.; Li, Z.; Hofmann, P. An undulator-based spherical grating monochromator beamline for angle-resolved photoemission spectroscopy. *Nucl. Instrum. Methods. Phys. Res. B* **2004**, *523*, 441.
- (54) Piamonteze, C.; Flechsig, U.; Rusponi, S.; Dreiser, J.; Heidler, J.; Schmidt, M.; Wetter, R.; Calvi, M.; Schmidt, T.; Pruchova, H.; Krempasky, J.; Quitmann, C.; Brune, H.; Nolting, F. X-Treme beamline at SLS: X-ray magnetic circular and linear dichroism at high field and low temperature. J. Synchrotron Radiat. 2012, 19, 661–674.
- (55) Hohenberg, P.; Kohn, W. Inhomogeneous electron gas. *Phys. Rev.* **1964**, *136*, B864–B871.
- (56) Blöchl, P. E. Projector augmented-wave method. Phys. Rev. B 1994, 50, 17953–17979.

- (57) Kresse, G.; Hafner, J. Ab initio molecular dynamics for liquid metals. Phys. Rev. B 1993, 47, 558-561.
- (58) Kresse, G.; Furthmüller, J. Efficient iterative schemes for ab initio total-energy calculations using a plane-wave basis set. *Phys. Rev. B* **1996**, *54*, 11169–11186.
- (59) Kohn, W.; Sham, L. J. Self-consistent equations including exchange and correlation effects. *Phys. Rev.* **1965**, *140*, A1133–A1138.
- (60) Lee, K.; Murray, E. D.; Kong, L.; Lundqvist, B. I.; Langreth, D. C. Higher-accuracy van der Waals density functional. *Phys. Rev. B* **2010**, *82*, 081101.
- (61) Becke, A. D. On the large gradient behavior of the density functional exchange energy.
 J. Chem. Phys. 1986, 85, 7184–7187.
- (62) Hamada, I. Van der Waals density functional made accurate. Phys. Rev. B 2014, 89, 121103.
- (63) Huttmann, F.; Martínez-Galera, A. J.; Caciuc, V.; Atodiresei, N.; Schumacher, S.; Standop, S.; Hamada, I.; Wehling, T. O.; Blügel, S.; Michely, T. Tuning the van der Waals interaction of graphene with molecules via doping. *Phys. Rev. Lett.* 2015, 115, 236101.
- (64) Perdew, J. P.; Burke, K.; Ernzerhof, M. Generalized gradient approximation made simple. *Phys. Rev. Lett.* **1996**, *77*, 3865–3868.
- (65) Anisimov, V. I.; Aryasetiawan, F.; Lichtenstein, A. I. First-principles calculations of the electronic structure and spectra of strongly correlated systems: the LDA + U method. J. Condens. Matter Phys. 1997, 9, 767–808.
- (66) Goedkoop, J. B.; Thole, B. T.; van der Laan, G.; Sawatzky, G. A.; de Groot, F. M. F.; Fuggle, J. C. Calculations of magnetic X-ray dichroism in the 3d absorption spectra of rare-earth compounds. *Phys. Rev. B* 1988, 37, 2086–2093.

- (67) Thole, B. T.; Carra, P.; Sette, F.; van der Laan, G. X-ray circular dichroism as a probe of orbital magnetization. *Phys. Rev. Lett.* **1992**, *68*, 1943–1946.
- (68) Carra, P.; Thole, B. T.; Altarelli, M.; Wang, X. X-ray circular dichroism and local magnetic fields. *Phys. Rev. Lett.* **1993**, *70*, 694–697.
- (69) Wu, R.; Freeman, A. J. Limitation of the magnetic-circular-dichroism spin sum rule for transition metals and importance of the magnetic dipole term. *Phys. Rev. Lett.* 1994, 73, 1994–1997.
- (70) Crocombette, J. P.; Thole, B. T.; Jollet, F. The importance of the magnetic dipole term in magneto-circular X-ray absorption dichroism for 3d transition metal compounds. *J. Condens. Matter Phys.* **1996**, *8*, 4095–4105.
- (71) Schumacher, S.; Huttmann, F.; Petrović, M.; Witt, C.; Förster, D. F.; Vo-Van, C.; Coraux, J.; Martínez-Galera, A. J.; Sessi, V.; Vergara, I.; Rückamp, R.; Grüninger, M.; Schleheck, N.; Meyer zu Heringdorf, F.; Ohresser, P.; Kralj, M.; Wehling, T. O.; Michely, T. Europium underneath graphene on Ir(111): intercalation mechanism, magnetism, and band structure. Phys. Rev. B 2014, 90, 235437.
- (72) Schröder, U. A.; Petrović, M.; Gerber, T.; Martínez-Galera, A. J.; Grånäs, E.; Arman, M. A.; Herbig, C.; Schnadt, J.; Kralj, M.; Knudsen, J.; Michely, T. Core level shifts of intercalated graphene. 2D Mater. 2016, 4, 015013.
- (73) Wang, X.-X.; Li, H.-N.; Zhang, W.-H.; Xu, F.-Q. Valence band of metal europium studied with synchrotron radiation photoemission spectroscopy. *J. Condens. Matter Phys.* **2007**, *19*, 096001.
- (74) Caspers, C.; Müller, M.; Gray, A. X.; Kaiser, A. M.; Gloskovskii, A.; Fadley, C. S.; Drube, W.; Schneider, C. M. Chemical stability of the magnetic oxide EuO directly on silicon observed by hard X-ray photoemission spectroscopy. *Phys. Rev. B* **2011**, *84*, 205217.

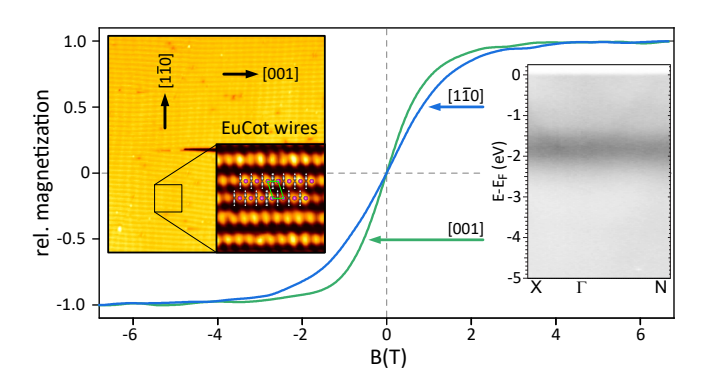


Figure 6: For Table of Contents Only.